SPACE WEATHER EFFECTS ON IMAGING DETECTORS IN LOW EARTH ORBIT

A Thesis

by

ADAM ALAN JOHNSON

Submitted to the Office of Graduate Studies of
Texas A&M University
in partial fulfillment of the requirements for the degree of

MASTER OF SCIENCE

August 2010

Major Subject: Aerospace Engineering

SPACE WEATHER EFFECTS ON IMAGING DETECTORS IN LOW EARTH ORBIT

A Thesis

by

ADAM ALAN JOHNSON

Submitted to the Office of Graduate Studies of
Texas A&M University
in partial fulfillment of the requirements for the degree of

MASTER OF SCIENCE

Approved by:

Chair of Committee,	Adonios Karpetis
Committee Members,	Tom Pollock
	Eric Petersen
Head of Department,	Dimitris Lagoudas

August 2010

Major Subject: Aerospace Engineering

ABSTRACT

Space Weather Effects on Imaging Detectors in Low Earth Orbit. (August 2010)
Adam Alan Johnson, B.S., Texas A&M University
Chair of Advisory Committee: Dr. Adonios N. Karpetis

The objective of this research is the statistical study of space weather effects on image detectors in Low Earth Orbit. The Hubble Space Telescope is used as a resource for acquiring proton affected images for statistical analysis. For the purpose of the present work, the space weather environment will consist of cosmic as well as solar proton particles. The proton occurrences evident in images from the Hubble Charge Coupled Device (CCD) have been used to calculate the probability of proton events, which is related to the local space weather particle flux. The proton particles transfer energy to the CCD silicon, which ultimately results in measured signal that is not originating from photon illumination. The signal due to the proton interactions is first separated from the noise contribution and subsequently used in the determination of a pulse height probability distribution. Separation of the noise from the proton events also leads to the measurement of proton streak lengths and orientations along with the associated probability distributions. The directionality of the space weather environment in Low Earth Orbit is examined using the distribution of proton streak angles. Statistics found from the Hubble are also used as a starting point for simulations that create synthetic proton signal images. The distributions resulting from the Hubble CCD analysis give the probability of the: number of proton events, which is related to the flux of the space weather protons; energy of proton events, which allows estimates of damaging proton interactions; length of proton streaks on the CCD, which shows the relative probability of a long traversing proton event; angle of proton event, which indicates the directionality of the space weather environment.

To Kristen

ACKNOWLEDGMENTS

I would like to thank my advisor, Dr. Adonios Karpetis, for pushing me to excel and my committee members, Dr. Tom Pollock and Dr. Eric Petersen, for taking interest in my research. I would also like to thank the Space Engineering Research Center for the fiscal ability to perform this research, and my research partners, Alex Bayeh, Celine Kluzek, and Tetsu Nakamura for their assistance and friendship. To my wife Kristen: you have made this time in my life exciting and fun, and I cannot thank you enough for your patience and support through everything. Finally, I would like to thank Vic, Barbara, Kara, Andrew, Steven, and the Holmstrom, Johnson, Turn, and Baker families. “Bless the LORD, O my soul, And all that is within me, bless His holy name.” - Psalms 103:1

TABLE OF CONTENTS

Page

LIST OF TABLES

LIST OF FIGURES

I. INTRODUCTION

A. Space weather

Our atmosphere can cause tornadoes, hurricanes, and tropical storms that can create havoc for people and their properties. Similarly, in space there is hazardous weather coming from the cosmos and our solar system that can damage space-borne instruments as well as earth-bound electronic instruments. Lundstedt [1] referred to space weather as "conditions on the Sun and in the solar wind, magnetosphere, ionosphere, and thermosphere that can influence the performance and reliability of space-borne and ground-based technological systems and can endanger human life or health." On April 21, 2002 the communication system on the Nozomi Mars Probe was disabled temporarily due to a high-energy space weather event[1]. Space weather can also cause malfunctions on earth. For example, in March 1989 a space weather storm caused the magnetic field of the earth to fluctuate rapidly which resulted in the failure of the Hydro Quebec power system[2] [2]. The failure caused a blackout in the province for nine hours.

Two of the common space weather elements that may cause malfunctions are solar protons and cosmic protons. Solar protons are particles that are ejected from the sun, which stream towards the earth with high velocities and energies. Most of the particles are deflected away from our planet by the magnetic field of the earth.

The journal model is *IEEE Transactions on Nuclear Science.*

[1] Keith Cowing, "Solar Flare Shuts Down Nozomi Mars Probe's Communication System" available online at http://www.spaceref.com.

[2] "In March 1989, Quebec experienced a blackout caused by a solar storm." available online at http://www.hydroquebec.com.

However some are entrained by the magnetic field to create the Van Allen radiation belts [3]. The particles that are entrained can penetrate into a satellite and interact with an electronic circuit that could potentially shut down the entire satellite. Cosmic protons carry even higher amounts of energy, moving at a fraction of the speed of light, and have similar damaging effects as solar proton particles [4].

The goal of this research is to analyze space weather effects on imaging detectors in Low Earth Orbit (LEO). One method for analyzing space weather effects on detectors is by exposing an imaging sensor, like a Charge-Coupled Device (CCD), to a proton or radiation source as shown in reference [5]. Difficulties with this approach include the cost of imaging sensors, the availability and access to proton and radiation sources, and the need to perform modeling and extrapolate the results from the experiments conducted on earth to the space weather environment. Another means of analysis is statistical modeling of actual space weather events as they take place in orbit, as shown in references [6, 7]. For this method the difficulties include the need for experimental data to validate models, the often complicated algorithms, and the associated extensive computational time.

The main innovation of the present work is the use of images from the Hubble Space Telescope (HST) Advanced Camera for Survey (ACS) to analyze the space weather environment in LEO. The Advanced Camera for Survey uses three charge-coupled devices to image the universe, and these are affected by space weather as will be shown in the next section. The advantages of using this approach are many: dark images, without *any* processing or illumination, are available; the images acquired have long exposure times, which allow for many proton events; NASA provided records, which give valuable information like position of spacecraft, date and time of picture, and pointing information; finally, the data can be freely downloaded from available archives, allowing us to perform our ‘experiments’ without cost.

B. Charge coupled devices

Charge-coupled devices are imaging detectors that are used in many space instruments, as well as many earth instruments. These focal plane arrays convert photons to binary counts in three steps: converting photons into electron hole-pairs; separating the electrons from the holes; collecting and reading the electrons [8]. The first step is completed by utilizing a semiconductor material, silicon, which will create an electron hole-pair when a photon with high enough energy interacts with it. The range of photon energy needed to create an electron hole-pair in silicon is $3.6eV$, corresponding to a wavelength of 344 nm, to $1.11eV$, or a wavelength of 1116 nm. [9, 10]. If an electron hole-pair is created, the separation of the negatively charged electrons and the positively charged holes is accomplished by applying an electric field across the semiconductor. After an amount of time, the electrons collected by the structure result in a charge that is transferred from pixel to pixel and finally through the Analog to Digital (A/D) converter to storage. Shown in Figure (1) is a diagram of a single pixel illustrating the silicon substrate, gate, and electron hole-pair.

The effect of space weather protons on CCD pixels is similar to the effect of photons on pixels. A high energy proton traversing the device will create electron hole-pairs by ionization or collisions [10, 11]. If the proton has a low incident angle with respect to the CCD plane, then the proton can cross multiple pixels, creating electron hole-pairs in each one, as illustrated in Figure (2). As with electrons created by photons, the electrons created by protons will be collected if inside the active region. The resulting image will have a long “streak” due to the proton passage, and not due to any illumination by photons. A dark image from the Hubble Space Telescope is shown in Figure (3), which includes proton streaks associated with the interaction with the CCD.

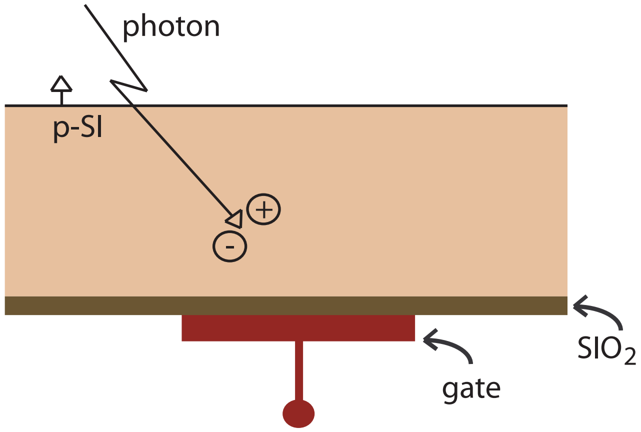

Fig. 1. Single pixel illustration from a back-illuminated CCD.

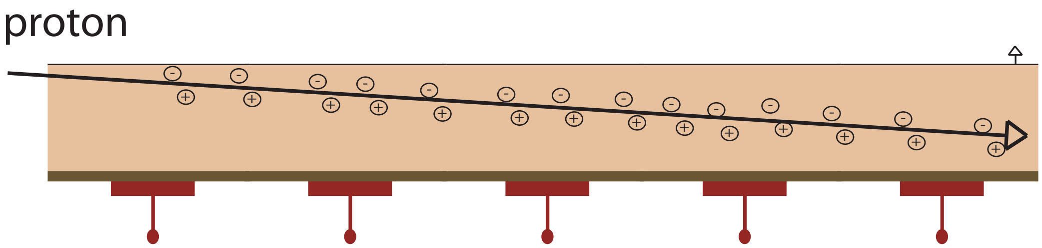

Fig. 2. Proton crossing multiple pixels generating electron hole-pairs.

C. Hubble Space Telescope

Named after the famous astronomer, Edwin Hubble, the Hubble Space Telescope (HST) is a low earth orbit telescope. Hubble is a NASA operating satellite, and as a consequence the academic community can freely acquire data from it. Allowing astronomers, scientists, and engineers to get data and pictures as requested. This accessibility also means that all of the processing done on the HST images must be described in detail, providing the acquiring party with infromation on what is filtered

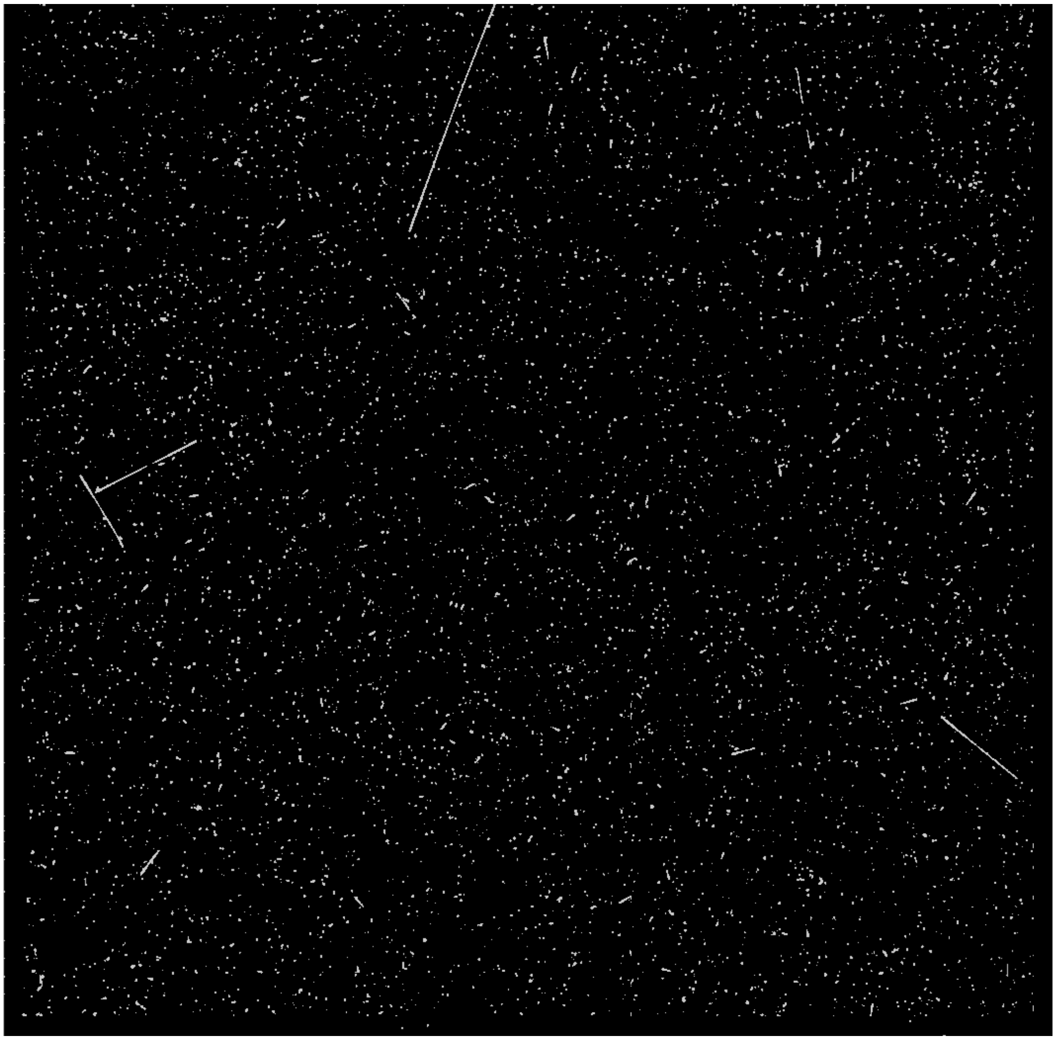

Fig. 3. Dark image from the Hubble showing proton streaks.

or changed from each raw image that is acquired. This section will give an overview of the Hubble Space Telescope, a detailed look into the camera used for space weather analysis, and describe how the dark images were acquired.

Since the start of operations, many generations of scientific instruments have been onboard the Hubble. Currently six scientific instruments are present: the Wide Field Camera 3 (WFC3); Near Infrared Camera and Multi-Object Spectrometer (NIC-

MOS); Cosmic Origins Spectrograph (COS); Advanced Camera for Surveys (ACS); Space Telescope Imaging Spectrograph (STIS); and the Fine Guidance Sensor (FGS)[3] [12]. Figure (4) shows the HST[4], while Figure (5) shows the currently installed systems.

Fig. 4. Hubble Space Telescope.

The images acquired from the Hubble archives are from the Advanced Camera for Survey. This instrument was chosen because of the large number of dark images that could be found in online NASA depositories. As will be shown subsequently, these images were used to extract information about proton events. The ACS instrument

---

[3] The FGS is used as a scientific instrument, measuring brightness and position of stars, when not guiding the telescope.

[4] NASA images homepage available online at http://www.nasaimages.org/

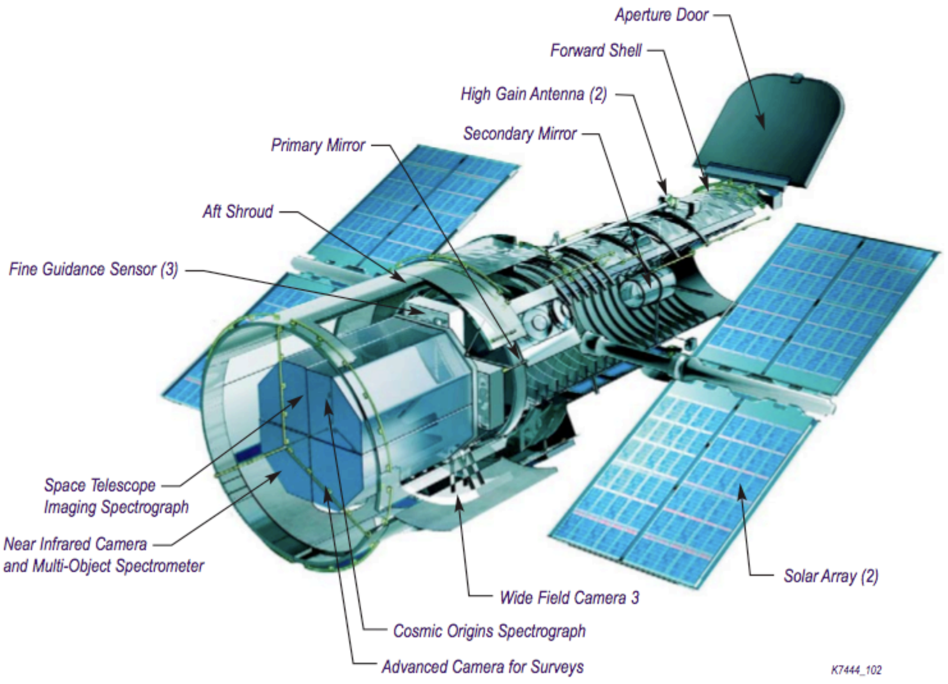

Fig. 5. Hubble Space Telescope systems diagram [12].

has three different cameras, two of which employ CCD chips. One is the Wide Field Camera (WFC), which has two 2048 × 4096 CCD chips that are butted next to each other, and the second is the High Resolution Camera (HRC). The HRC instrument became inactive after a short-circuit event in 2007 and was the only instrument that was not repaired during the STS-125 servicing mission. Even though this CCD was only active during five years, from 2002 to 2007, numerous images exist that can be used for space weather analysis.

The High Resolution Camera (HRC) uses a single 1024 × 1024 pixel CCD array with $21\mu m$ pixel size. The CCD is a back-illuminated unit that was produced by Scientific Imaging Technologies (SITe) and was optimized for near-UV spectrum illumination, as evidenced by its quantum efficiency, shown in Figure (6) [13, 14, 15, 16].

Table I shows some of the parameters of the HRC charge-coupled device, which are important to the generation of proton signal statistics.

Table I. High resolution cameras CCD properties [13, 14, 15, 16].

Imaging Array Format	1024×1024
Pixel Size	21 μm x 21 μm
Operating Temperature	$-80°$C
Full Well Capacity	$150,000\ e^-$
Depletion Depth	7 μm
Normal Dark Current	0.005 e^-/s
Read Noise	4.7 e^-

The dark images acquired from the Hubble Space Telescope archives, are found on a web site called Multimission Archive at STScI (MAST[5]). The archives are a component of the NASA distributed Space Science Data Services (SSDS). To search through the archives and gain access to the MAST, a program called StarView[6] was used. StarView is a Java-written program that allows users to search the MAST archives for data, calibration information, and proposal information. This program was used to search for Hubble pictures that are dark images. StarView allows users to mark data to be downloaded securely from a File Transfer Protocol (FTP) source.

The position of the Hubble above the earth, in Geocentric coordinates, was also

---

[5] MAST archive main homepage available online at http://archive.stsci.edu.

[6] StarView main homepage available online at http://starview.stsci.edu/html/

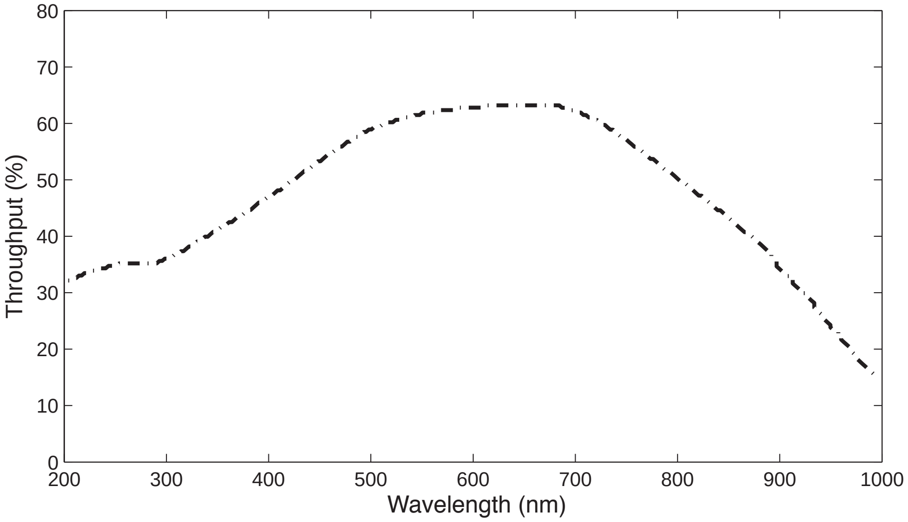

Fig. 6. Measured quantum efficiency of the HCR [13].

determined. This was essential for the determination of the local space weather conditions, and specifically the inhomogeneity and anisotropy of the proton flux. The position of the Hubble was found from the Jet Propulsion Laboratory (JPL) ephemeris, which utilizes a web-based program, named HORIZON[7], created by the Solar Systems Dynamics Group. This program allows high accuracy position data to be transferred via e-mail request. The retrieved position data is the latitude and longitude of the Hubble in a geocentric reference frame. The data was plotted, using Google maps and LabView, in order to observe the position of the Hubble while taking a single dark image. Figure (7) shows a screen shot from the LabView program along with the Hubble trajectory during acquisition of one dark image.

The orbit of the Hubble puts the telescope into a high activity space weather environment, the South Atlantic Anomaly (SAA), multiple times per day. This high

---

[7] The HORIZON main web portal program is available online at http://ssd.jpl.nasa.gov/horizons.cgi

Fig. 7. Hubble (H) trajectory (red) while taking one dark image, plotted onto Google maps.

radiation area over the atmosphere of the earth is a result of the asymmetric magnetic field of the earth [17]. The region can create problems for satellites because of the large particle fluxes as well as the intense radiation environment that prevail. Because of the risk for catastrophic instrument failure, caused by space weather, most satellites will go into a safe mode while traversing the SAA, including the Advanced Camera for Survey. The Hubble position was calculated in order to explore whether the highly energetic region, SAA, affected the images acquired.

II. RESULTS AND DISCUSSION

This section describes the methods of analysis and results performed on the dark images from Hubble. Statistical methods are used to calculate: (a) probability of the number of proton events; (b) probability of proton dark signal levels; (c) probability of proton streak lengths; (d) probability of proton streak orientations. The most fundamental of these probabilities is the number of proton events, which should follow arrival statistics. The interaction of the protons with the silicon substrate generates higher electron counts than noise from the CCD. This results in the total dark signal, i.e. signal accumulated on the detector in the absence of *any* illumination, showing a bimodal distribution from noise and proton streaks. The bimodality of the dark signal allows for the separation of proton streaks and detector noise. Eliminating the noise contributions allows for the measurement of proton streak lengths and orientations. In addition, this section describes algorithms for simulations that create synthetic proton streak images and their results. Monte Carlo techniques, utilizing the Metropolis algorithm, are implemented to generate images with the same underlying proton statistics as the Hubble images.

A. Probability of proton events

In many physical processes the rate of arrival events is equal to a flux[8], which in itself depends on the underlying physics of the problem. The protons penetrating through the CCD have a flux associated with them, which is calculated by knowing the number of proton events, CCD size, and exposure time for each image.

A Poisson distribution describes the physical process of arrival statistics when-

---

[8] The amount that flows through a *unit area* per *unit time.*

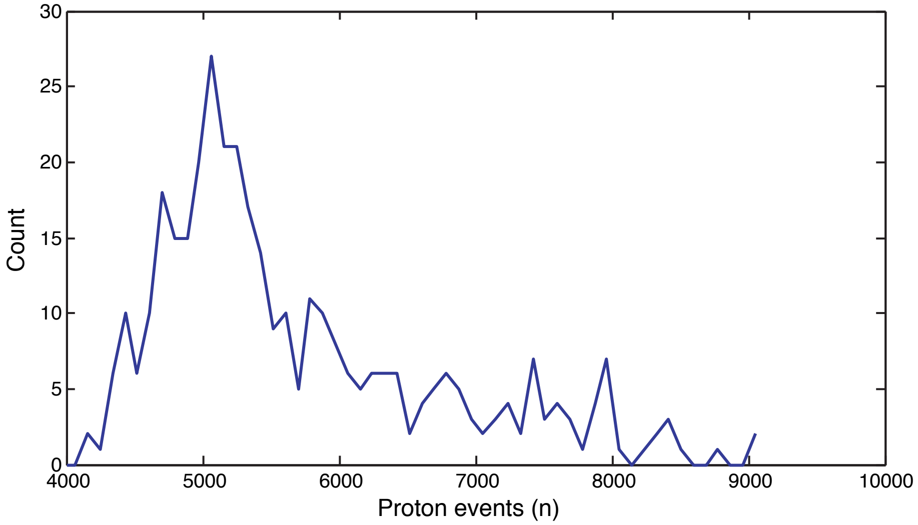

Fig. 8. Distribution of the number of proton events, area 1024 × 1024 pixels.

ever there is an average rate or flux λ [18, 19]. The Poisson is an example of a univariate distribution, since the arrival statistics can completely be described by a single variable, λ, which is equal to both the mean and the variance of the distribution. An example of a Poisson process is as follows: if a person stands by the side of the road and counts cars as they go by for ten minutes, repeating the process twenty times, the distribution of the number of cars per ten-minute period would follow a Poisson distribution. In this example the rate of the cars would equal λ. Shown in equation (0.1) is the Poisson function presenting dependence on one variable λ. Similarly protons arriving at the CCD with a flux are expected to follow a Poisson distribution.

$$P(x) = \frac{\lambda^x}{x!} e^{-\lambda} \tag{0.1}$$

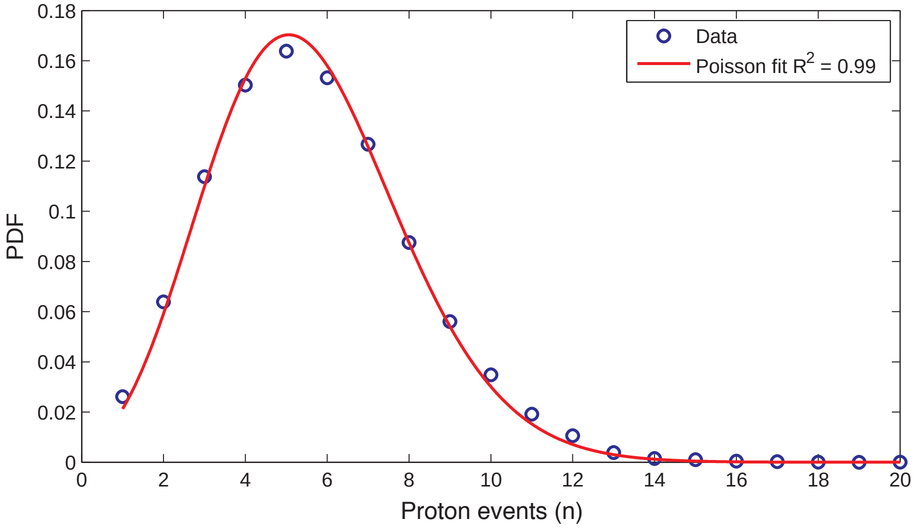

Fig. 9. Distribution of the number of proton events, area 32 × 32 pixels.

Analyzing the images from Hubble confirms that proton interactions produce higher signal levels than noise from the CCD[9]. The difference in signal distinguishes protons from noise and therefore proton counting can be accomplished for each image. As stated earlier, the number of proton events in each image should follow a Poisson distribution. Counting each proton event of the 365 images produces Figure (8), which does not show adequate convergence to any known distribution. Resemblances to a Poisson are apparent, however to conclude with any confidence more data is required. Since additional images could not be acquired and the integration time could not change, the solution to this problem is to divide the images into smaller sub-areas. The original image size is 1024 × 1024 pixels which is divided into smaller areas of 32 × 32 pixels. Decreasing the area decreases the total number of proton counts per area but at the same time increases the number of images and consequently statistics.

---

[9] Gaussian noise, described in depth in the next section.

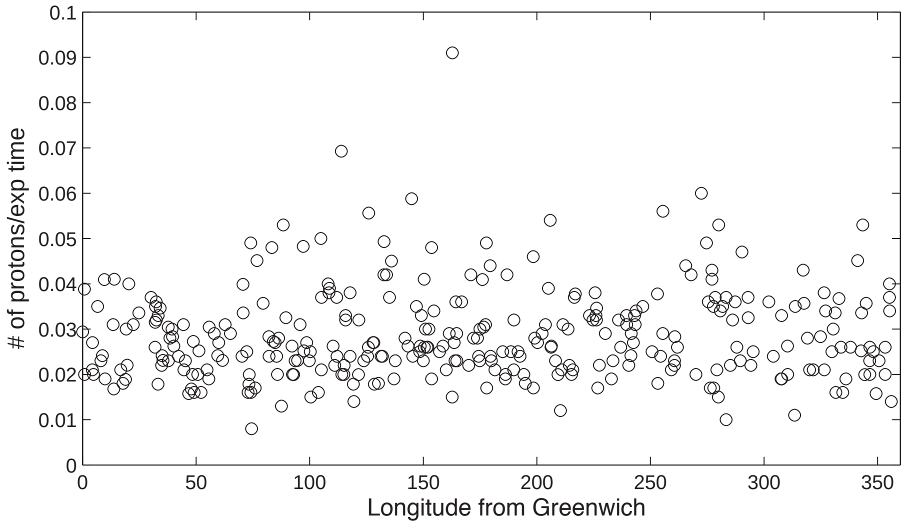

Fig. 10. Number of proton events versus longitude of earth. Results from all 365 images acquired from HST.

The result is shown in Figure (9), which shows a good correlation between the proton events and a Poisson distribution, e.g. $R^2 = 0.99$.

Different areas over the earth have inherently different proton fluxes, with the notable example of the South Atlantic Anomaly (SAA). The images acquired from the Hubble archives are from three different dark image sets, taken when the Hubble is in occultation, i.e. with the earth between the Hubble and the Sun. For this reason the position of the Hubble was found while taking the 365 images. To study the change in flux with respect to Hubble position, the number of proton events are calculated at the different earth longitudes. Each images has a total number of proton events that is counted for streak lengths greater then ten pixels long, which is subsequently normalized by the exposure time of the camera, i.e. 1000 seconds. The average number of proton events, greater then ten pixels long, is approximately 25. Shown in Figure (10) is the number of proton events normalized with the exposure time of the

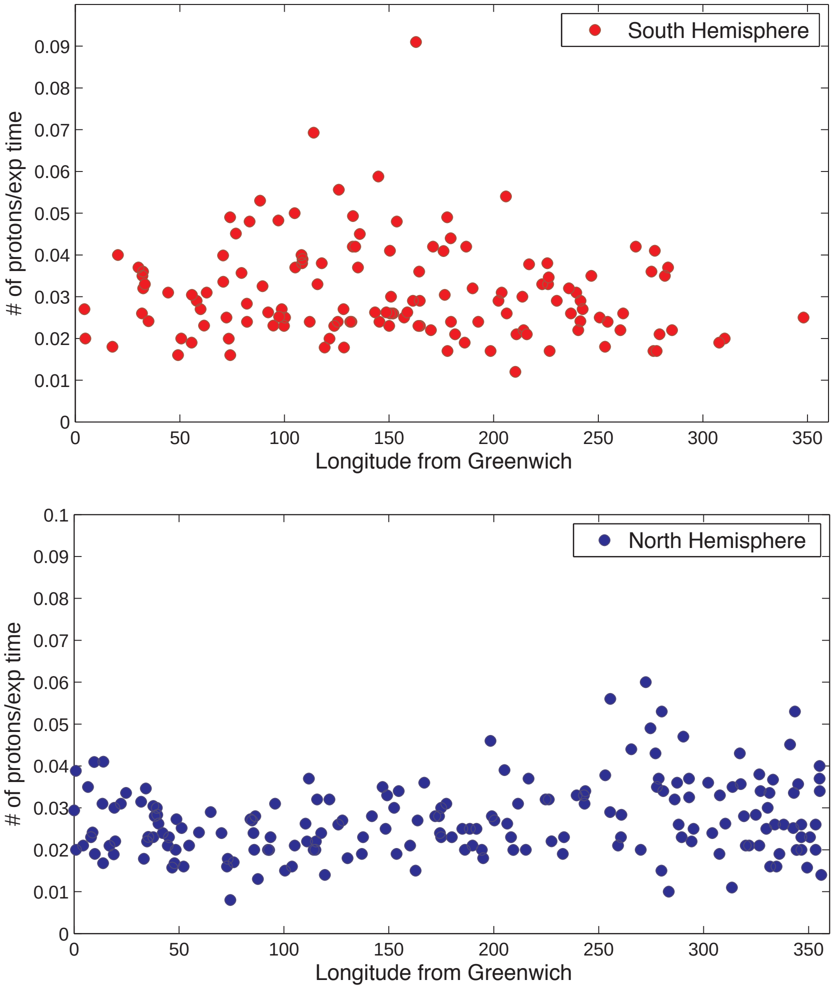

Fig. 11. Number of proton events versus longitude of the earth and hemisphere.

camera versus the longitude of the earth.

Figure (10) shows that the number of proton events does not depend strongly on longitude. Also this figure does not show any clear effect from the South Atlantic Anomaly, which resides in the approximate range from 270° to 70°. Knowing that the SAA should have an effect, the latitude was correlated with the number of proton events as well. Shown in Figure (11) is number of proton events south and north of the equator, versus longitude. These figures show that most of the higher proton events were in the south hemisphere, and images close the SAA are mostly in the north hemisphere.

Since the number of images is limited to the 365 found from the archives, the statistics of the number of proton event cannot be conditioned for the longitude and latitude of the Hubble. However, a binary condition can be made for images inside and outside the SAA, which assumes a high space weather region inside the anomaly and a uniform space weather region outside. Since the Hubble shuts down while traversing the SAA, all the images acquired are outside this region. For this reason the images from Hubble are considered to be captured in a low, uniform space weather environment. These results mean that the statistics can be accomplished on all 365 images for the probability of energy, length, and orientation of proton events.

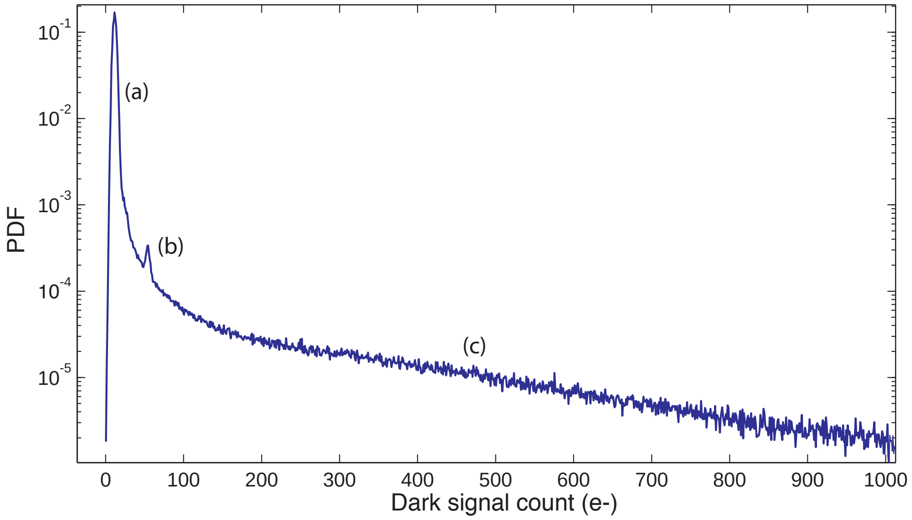

Fig. 12. PDF of dark signal count logarithmic ordinate.

B. Probability of dark signal levels

Energy deposited onto the CCD by the proton events has its own distribution of dark signal, i.e. dark electrons. These proton generated electrons are coupled with the electron noise from the CCD. The resulting total dark signal, recorded in each of our images, is a combination of CCD noise and proton generated electrons.

A histogram is made from the total signal counts from twenty dark images. The histogram data was converted into a Probability Density Function (PDF[10]) giving the relative frequency of signal counts. Figure (12) shows a PDF of dark signal counts from Hubble using an ensemble of twenty images out of the 365.

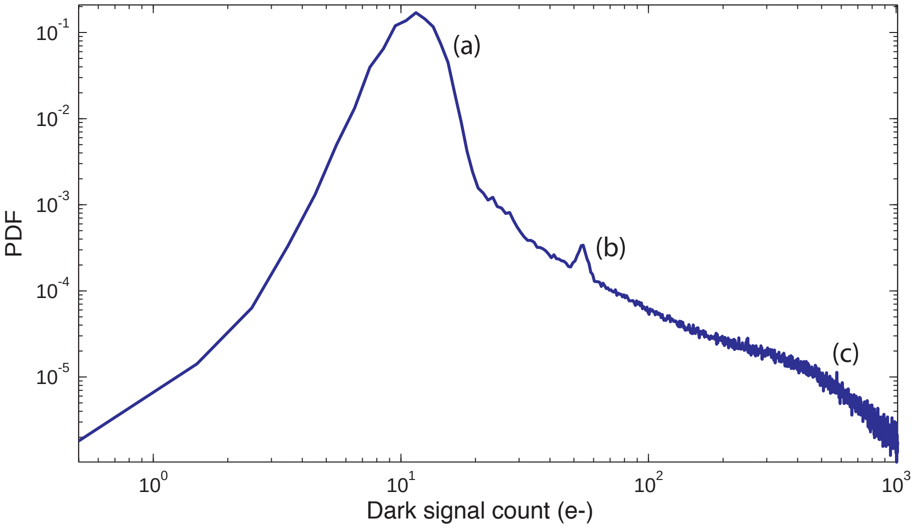

Fig. 13. PDF of dark signal count in logarithmic coordinates.

---

[10] The definition for the probability density function is $PDF(x) = f(x)/\int_0^\infty f(x)\,dx$ The function $f(x)$ is the histogram of signal counts, which is converted into a PDF by forcing a unit area under the function curve over the total data interval.

Figure (12) shows a large peak at an approximate value of 10 counts, signifying that this is the most probable value of pixel 'intensity' in the dark images. To further analyze the distribution of the dark signal, the PDF is plotted in a log-log graph shown in Figure (13). Figure (13) shows three distinct features: (a) the large peak at small values of signal ≈ 10; (b) a second peak at approximately 50 counts; (c) an apparent exponential decay for high values of signal. Feature (b) is due to a distinct trait that is present in all twenty images. This trait is due to a region of 7×1024 pixels on the CCD that consistently exhibit relatively high pixel counts. The relatively higher pixel counts could be due to a CCD amplifier or a thermally hot region of the CCD chip. Therefore this feature is considered an artifact of the CCD and not important to this study. Figure (14) shows the artifact of the CCD, located on the left side of the inverse image, under high contrast conditions.

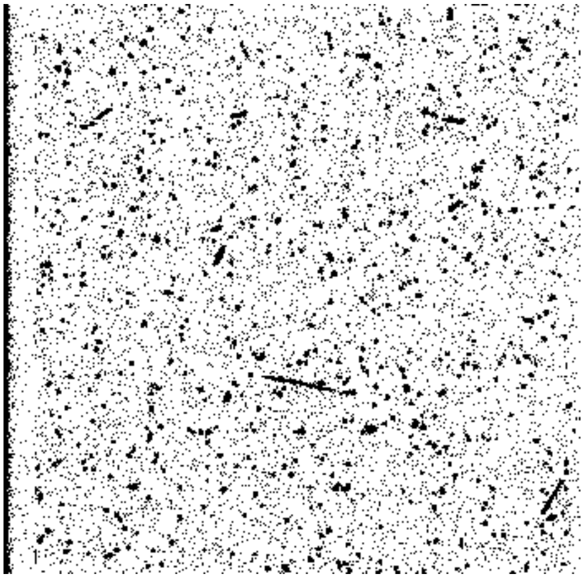

Fig. 14. Inverse image from Hubble showing the CCD artifact.

To discover the underlying distribution of the other two features, (a) and (c), the different regions of the PDF were fitted with diverse distributions. For the small signal values, the expected distribution is Poisson from dark current and Gaussian from read noise. Dark current is noise generated from the silicon of the CCD, which is caused from thermally activated electrons inside the depletion layer. This is expected to follow a Poisson process because the rate at which the electrons are generated and collected is constant, thus signifying arrival statistics. [8, 20]. Read noise is created through the movement of charge between pixels, amplifier, and the Analog to Digital converter (A/D). Figure (15) is a diagram showing the different sources of electrons in CCD. As illustrated in the figure, the total signal acquired is a combination of proton generated electrons (Pe^-), dark current generated electrons (De^-), and read noise (Re^-).

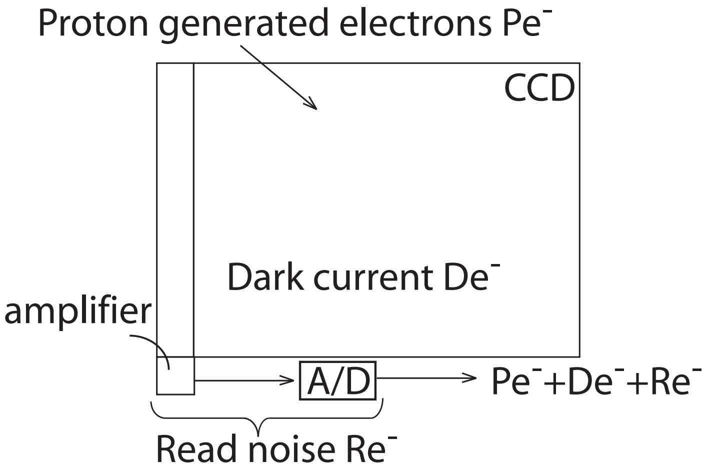

Fig. 15. Diagram of electron sources collected form the CCD.

Initially the first feature (a) was fitted with a Gaussian, as shown in Figure (16). The Gaussian fit follows the data of the PDF with a coefficient of determination

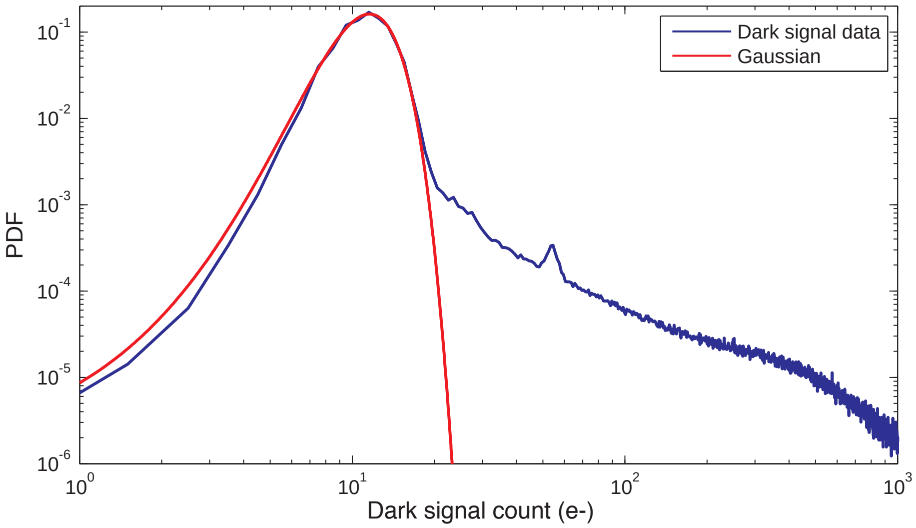

Fig. 16. PDF of dark signal count with Gaussian fit.

$R^2 = 0.99$. This is considered an excellent fit in most cases, however Figure (16) shows that the Gaussian fit does not explain the other feature, namely the decay at large signal values.

A Poisson distribution was also fitted to the small values of the PDF to determine which is a more accurate approximation. The PDF of dark signal with the Poisson fit is shown in Figure (17), which shows that a Poisson fit does not capture the signal decay better then the Gaussian fit. In addition, the coefficient of determination is lower for a Poisson than the Gaussian, e.g. $R^2 = 0.91$, signifying that a Poisson distribution is not a particularly good fit to the low signal levels.

The third distribution fitted to the PDF at small values was a Gamma distribution, which is a two-parameter distribution related to the Poisson. These two-parameters are λ, which is equal to the expected rate of arrivals, and α, which is the number of arrivals in a certain waiting time. The PDF with the Gamma fit is

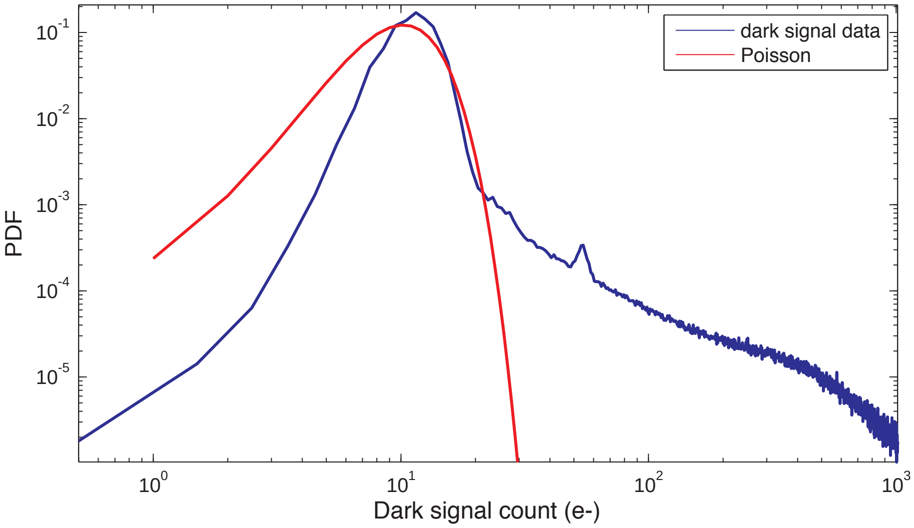

Fig. 17. PDF of dark signal count with Poisson fit.

shown in Figure (18). The coefficient for the Gamma distributions is $R^2 = 0.95$. The Gamma fits the first feature better than the Poisson but still does not account for the decay at large signal values. Furthermore, the Gamma distribution requires two adjustable parameters, like the Gaussian. The latter offers a much better fit to the low-level signal PDF.

The PDF at large values was fitted with an exponential function in the interval 200-1000, as shown in Figure (19). The coefficient of determination for the exponential fit within the interval 200 to 1000 is $R^2 = 0.97$. This fit exhibits an excellent correlation with the large signal values.

One single distribution was not found to explain both features (a) and (c), which indicates the presence of different physical mechanisms for each feature. The first feature (a) is best described by a Gaussian, which indicates that this feature is due to the multiple noise factors, dark current, charge-transfer, amplifier(s), and Analog-to-

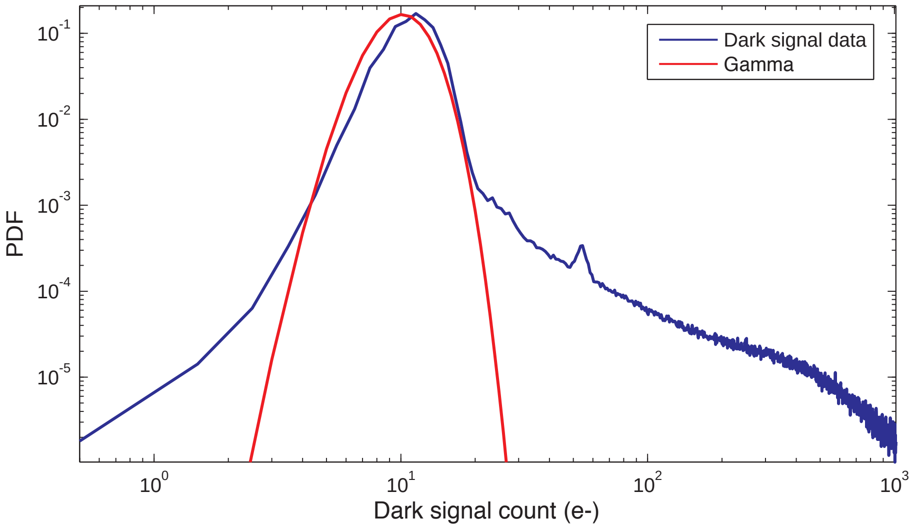

Fig. 18. PDF of dark signal count with gamma fit.

Digital (A/D) converter. We can supplement the quantitative description with actual numbers in what follows. The Gaussian feature has a mean equaling approximately $11e^{-}$, as shown in Figure (16). This mean value correlates well with the published characteristics of the CCD, seen in Table I. For the exposure time of 1,000 seconds, we expect the generated electrons from dark current to equal $0.005\frac{e^{-}}{sec} \times 1,000sec = 5e^{-}$. This is the mean value of thermally generated dark current, and we expect a Poisson distribution around this value to obtain. At the same time, each pixel charge is 'suffering' the read noise of approximately $4.7e^{-}$, on average. Hence, an average value of $9.7e^{-}$ is anticipated for the electron counts in the absence of any proton events. This value is quite close to the measured one $(11e^{-})$ and, in general, a higher value is expected in the actual images, precisely due to the presence of the proton events [20, 21]. The Gaussian feature has also shown up in reference [22], which describes data from the Wide Field Camera 3 on the Hubble held at a temperature

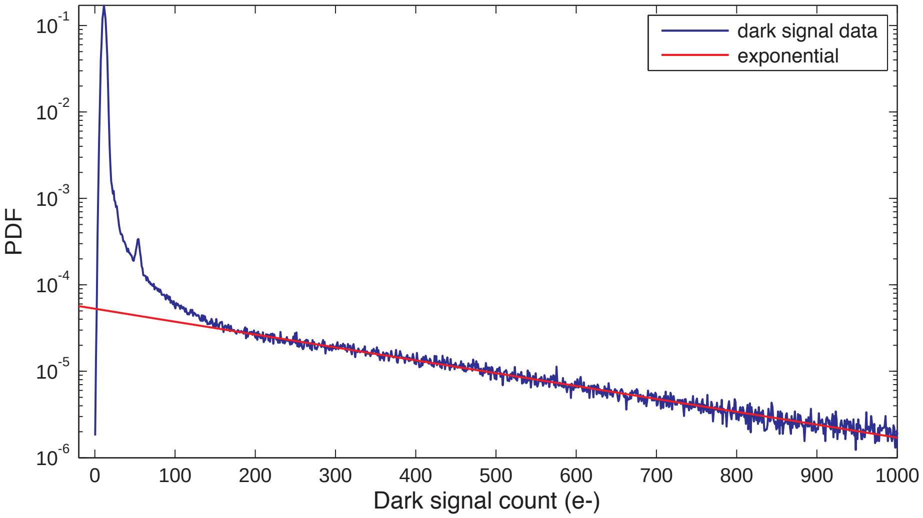

Fig. 19. PDF of dark signal count with exponential fit.

of $-85°C$.

The large values show an excellent correlation with an exponential decay, which is present in many literature references [5, 21, 23, 24] for different imaging arrays. The decay is also present in recent work by Henley that uses Monte Carlo simulations to generate dark signal from proton interactions on a CMOS chip [25]. Monte Carlo simulations have also generated the exponential decay in references [26, 27]. The hypothesized mechanism that creates the exponential decay is transient effects. These effects are protons ionizing the active region of the CCD array creating electron hole-pair, which is dependent on the Linear Energy Transfer (LET), or ionizing energy loss (dE/dx), of the proton. The distribution from these transient effect have been modeled in reference [7], which also resulted in an exponential distribution.

Summarizing the dark signal distribution based on the observations and the literature: feature (a) is due to multiple noise mechanisms from the CCD that results in a Gaussian distribution; feature (b) is a artifact of the CCD and deemed not important to this study; feature (c) is a exponential decay that has been explored in other work and is due to multiple proton effects. Work attempting to construct a two-parameter PDF, with one parameter being the dark signal counts and the other being proton streaks lengths is ongoing. The resulting two-parameter PDF would give further insight into the possible correlation between dark count levels and streak lengths.

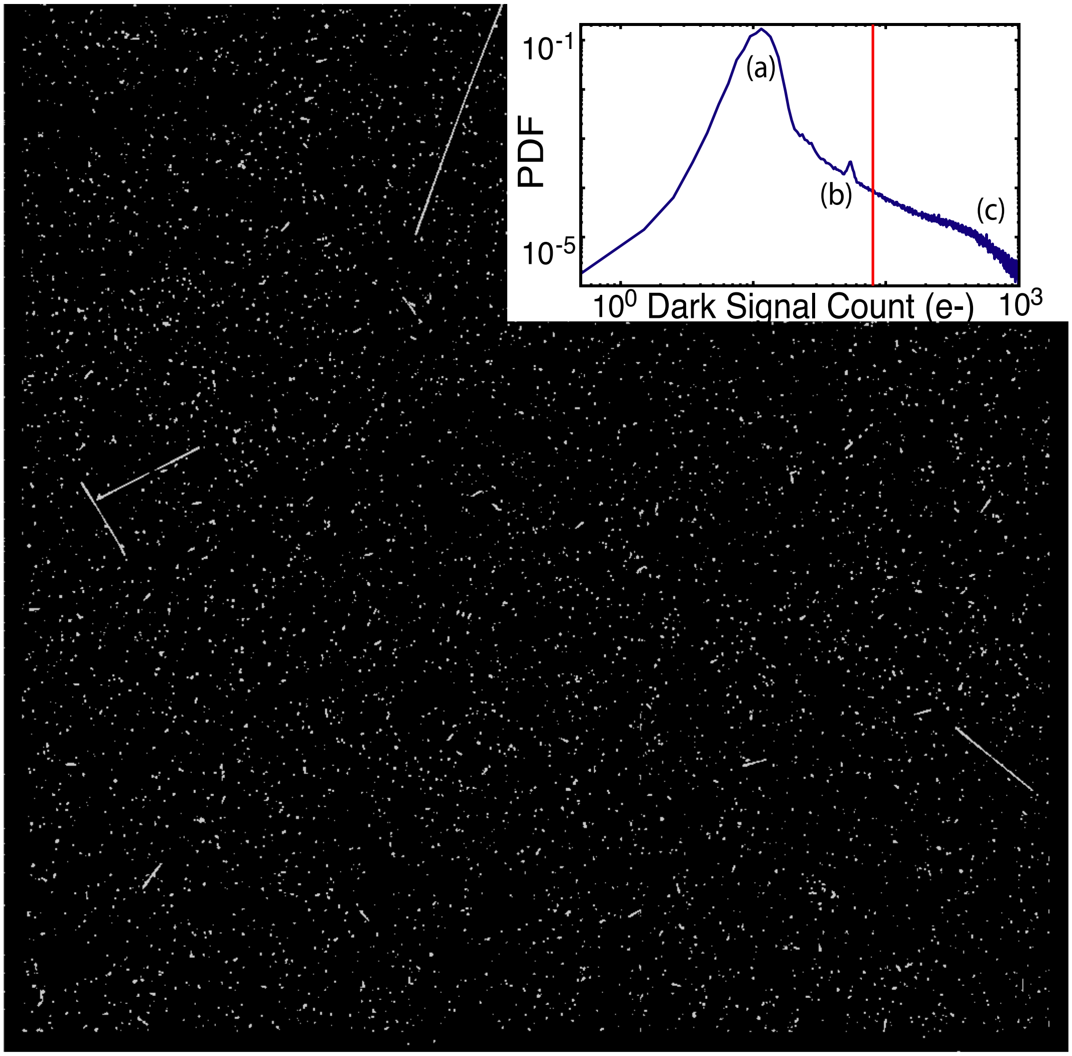

Fig. 20. (a) Hubble image with cutoff filter and (b) the dark signal with cutoff value.

C. Probability of proton streak lengths

The results from the dark signal analysis show that the exponential feature (c) is due to proton interactions. An assumption that energies higher then some dark signal value[11] is employed to differentiate the proton events from noise, which is needed to calculate streak lengths. This value, placed at transition from the artifact feature to the exponential feature, creates objects that can be measured in the image. The filter value was chosen because it eliminates features (a) and (b), while keeping the proton feature (c). This differentiation binarizes the images by assigning a value of one to proton events and a value of zero to other features, such as our CCD noise. Figure (20) shows the dark signal with the red line indicating the approximate cutoff value and the resulting binary image.

LabView Machine Vision software was employed to program algorithms for image analysis. One of the resulting programs that was used extensively calculated the proton streak lengths, by using the Pythagorean theorem ($r^2 = m_y^2 + n_x^2$), and the number of pixels in the vertical (m_y) and horizontal direction (m_x). The algorithm calculates the length of all objects that have a numeric value of one, set after binarization.

The length of each proton streak from the 365 images is used to create a probability density function (PDF) for streak lengths, which is shown in blue in Figure (21). This PDF is analyzed to determine the analytical form of the distribution. A nonlinear least squares method is used to fit the Hubble data to a power law, with the form $PDF(L) = \xi_1 L^{\xi_2}$, and solve for the constants, $\xi_1 = 8.01$ and $\xi_2 = -3.56$.

$$PDF(L) = \xi_1 L^{\xi_2} = 8.01 \times L^{-3.56} \tag{0.2}$$

---

[11] This value is approximately 70 signal counts above the minimum count value.

The power law fit is applied to streak lengths in the interval of ten to one hundred pixels. This interval is chosen because the smaller lengths, below ten pixels, have a higher susceptibility to the Gaussian noise. The interval stops at streaks of one hundred pixels because the data becomes unreliable due to low number of samples. The fitted power law is also plotted in red on Figure (21). The coefficient of determination within the interval is equal to $R^2 = 0.99$. Figure (21) is plotted in logarithmic coordinates, with confidence bounds at 95%.

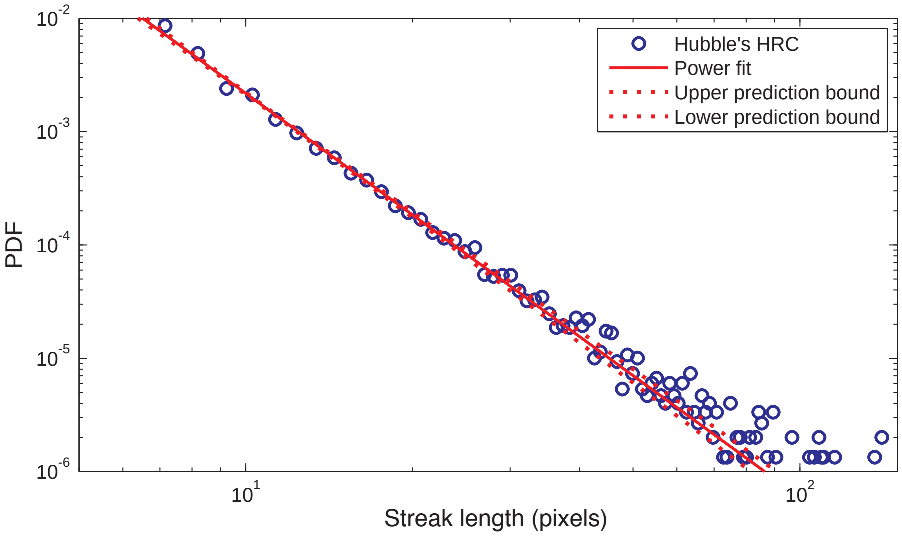

Fig. 21. Probability density function of streak lengths with power law fit.

The Gaussian noise from the CCD can not be completely rejected using a simple subtractive cutoff filter. Therefore, the possibility exists that noise affects the fitted power law exponent. Different cutoff filters were implemented to examine the sensitivity of the exponent to the cutoff filter. Shown in Figure (22) is the PDF of proton streak lengths for different signal cutoffs. The slopes of each line and their

95% confidence intervals are shown in Table (II). The table shows that a value of −3.56 is inside all but one of the confidence intervals. As shown in Table (II), even a substantial variation of the cutoff signal values does not lead to significant variation of the power law fit exponent. In what follows, a value of −3.56, the median of all the slope values, will be considered representative of the power law slope, and the corresponding value of cutoff filter, 70, will be sufficient to separate proton streak occurrences from noise on the CCD.

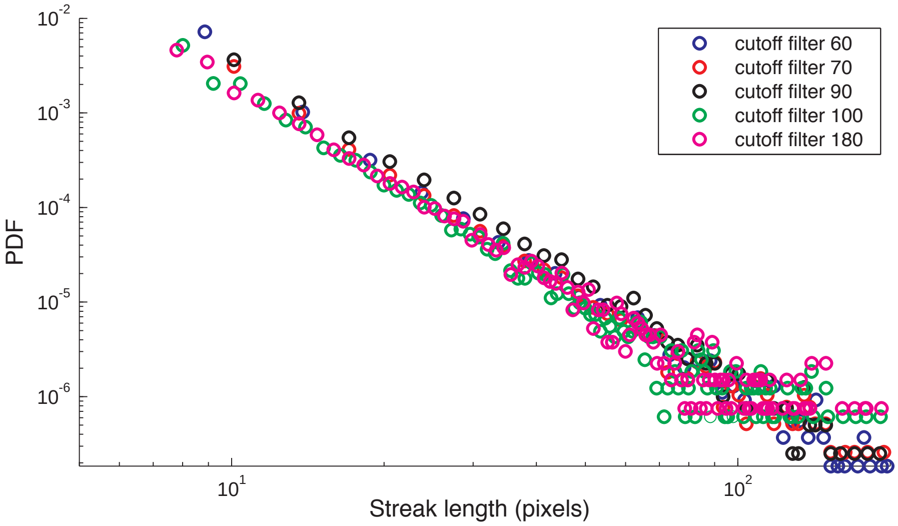

Fig. 22. Proton streak lengths with different cutoff filters.

Table II. Streak length power law slope for different cutoff filters.

Cutoff filter value	Slope	95% Confidence intervals for slope
60	-3.77	(-3.52, -4.02)
70	-3.56	(-3.46, -3.66)
90	-3.42	(-3.36, -3.47)
100	-3.57	(-3.34, -3.80)
180	-3.49	(-3.32, -3.66)

D. Probability of proton streak orientation

The orientations of the proton streaks are analyzed to determine if there is proton flux anisotropy, i.e. if there is directional dependence in our data. Reference [28] shows that flux anisotropy exists in the South Atlantic Anomaly (SAA) region of the Hubble orbit. However the images acquired from the Hubble are captured throughout its orbit and outside the SAA. The regions outside the SAA have an isotropic flux, which leads to the expected orientation distribution to exhibit a directionally independent result.

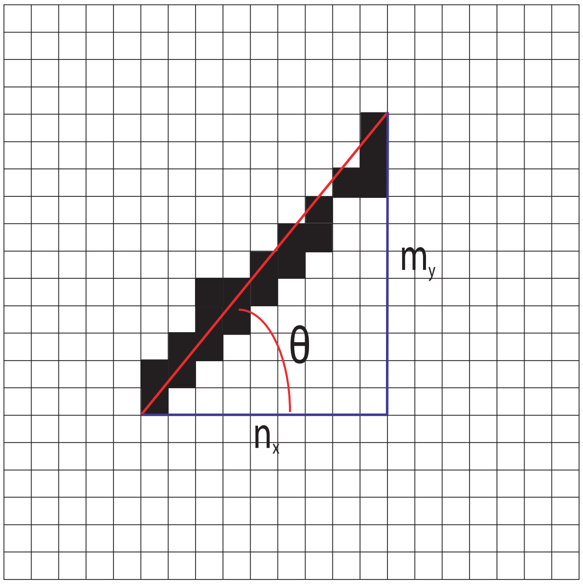

Fig. 23. Evaluation of proton streak orientation.

As shown in Figure (23), the orientation of each proton streak is measured from the horizontal axis of the image plane. The resulting orientation angle is calculated as $\arctan(m_y/n_x)$ [29], where m_y and n_x are the lengths of the proton streak in the vertical and horizontal directions, respectively. The angle calculated is used to obtain the PDF of proton streak orientations, as shown in Figure (24). The results were obtained by processing 365 images from Hubble, and considering all possible streak lengths.

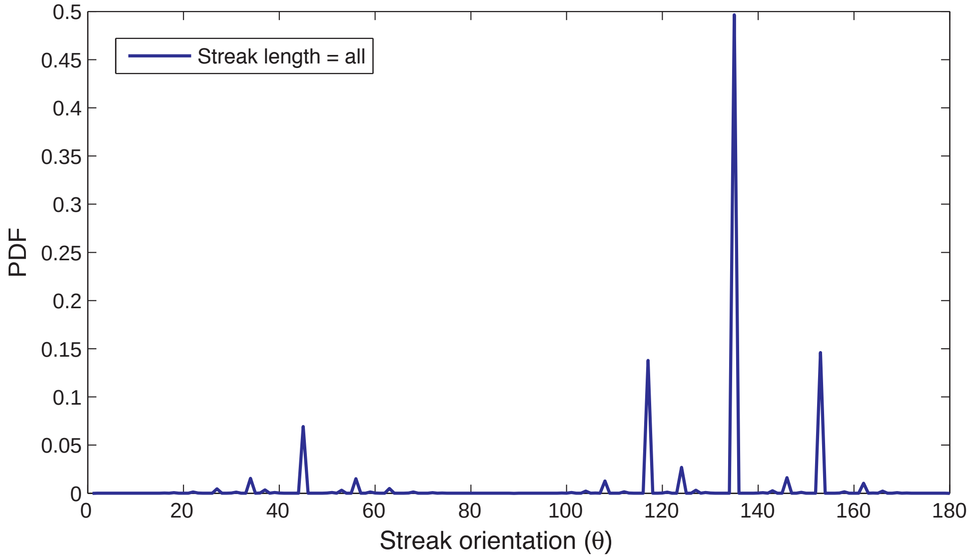

Fig. 24. PDF of proton streak orientations from Hubble.

Figure (24) indicates that most proton angles are equal to 135°, 116.7°, and 153.4°. The diagram in Figure (23) shows that the orientation of the streak is calculated by taking into account the corners of a pixel [29], which means that a single pixel will result in a streak length of $\sqrt{2}$ pixel lengths. The corner location also means that a single pixel will represent a streak angle of 135°. Figure (25) shows the pixel event combinations along with enumerations and all possible angles from the orientations illustrated. The diagram exhibits that the pixel combinations of 1×1 and 2×2, which are more probable, give rise to streak angles in the same values as the high spikes in Figure (24). This result would indicate that the larger spikes are mostly due

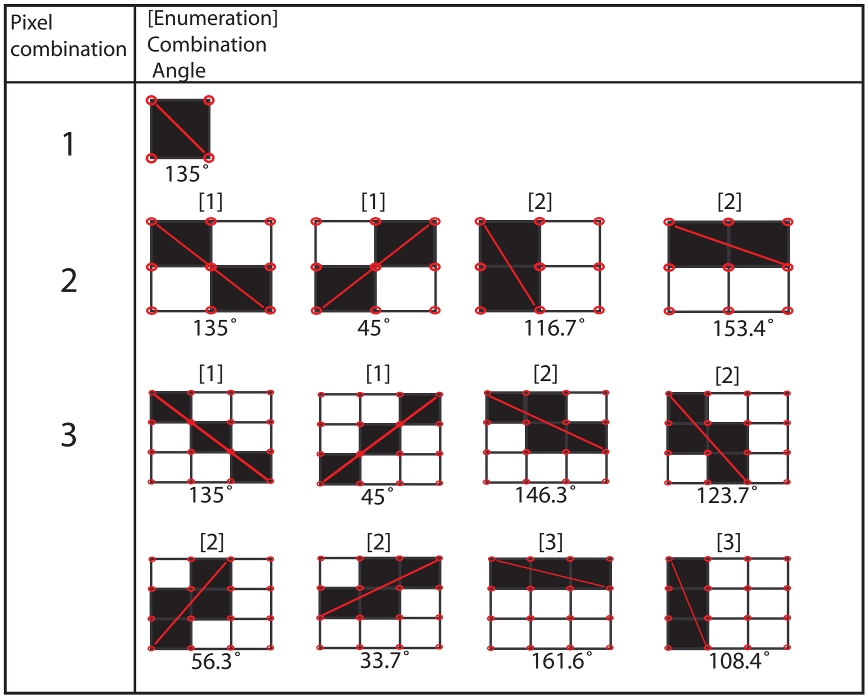

Fig. 25. Pixel combinations and corresponding orientation angle.

to smaller pixel combinations.

As already discussed in the previous sections, the dark current and read noise contributions expected to dominate the electron counts of single pixel events. Conversely, single pixel events are unlikely to correspond to proton events, as this would require proton strikes that are close to perfectly perpendicular to the CCD, and have no energy diffusion between pixels. Therefore, we expect small pixel combinations (e.g. 1×1 and 2×2) to correspond predominately to Gaussian noise and not proton events. To differentiate between the two, the orientation PDF is calculated with three different length cutoffs: (a) all the orientations without any length cutoff; (b) a cutoff equal to 3 pixel lengths; (c) a cutoff equal to 5.7 pixel lengths. The filter (b) value was chosen so that pixel combinations of 1×1 and 2×2 are eliminated. In addition, the value for filter (c) is set to eliminate all four-pixel combinations (4×4), along with some five-pixel combinations (5×5). Eliminating those pixel combinations allows for analysis of orientations from proton streak events and suppresses the possibility of Gaussian noise contributing to the orientation PDF.

Figure (26) presents the orientation PDF with the three length cutoffs: the cutoff value of zero, Figure (26a); the cutoff value of 3, Figure (26b); and the cutoff value of 5.7, Figure (26c). The figure shows that as the event streak length increases the orientation distribution tends towards symmetry around 90°. This is the case regardless of the type of event taking place, i.e. proton strike or noise. Since CCD noise contributes to the PDF in small pixel combinations, the longer streak events are due to proton streaks. This reasoning leads to the conclusion that the apparent symmetry around 90°, shown in Figure (26c), is because the proton particles arrive at the CCD without any directional preference. As already mentioned, such isotropy in proton flux is expected outside of the SAA regions along the Hubble orbit.

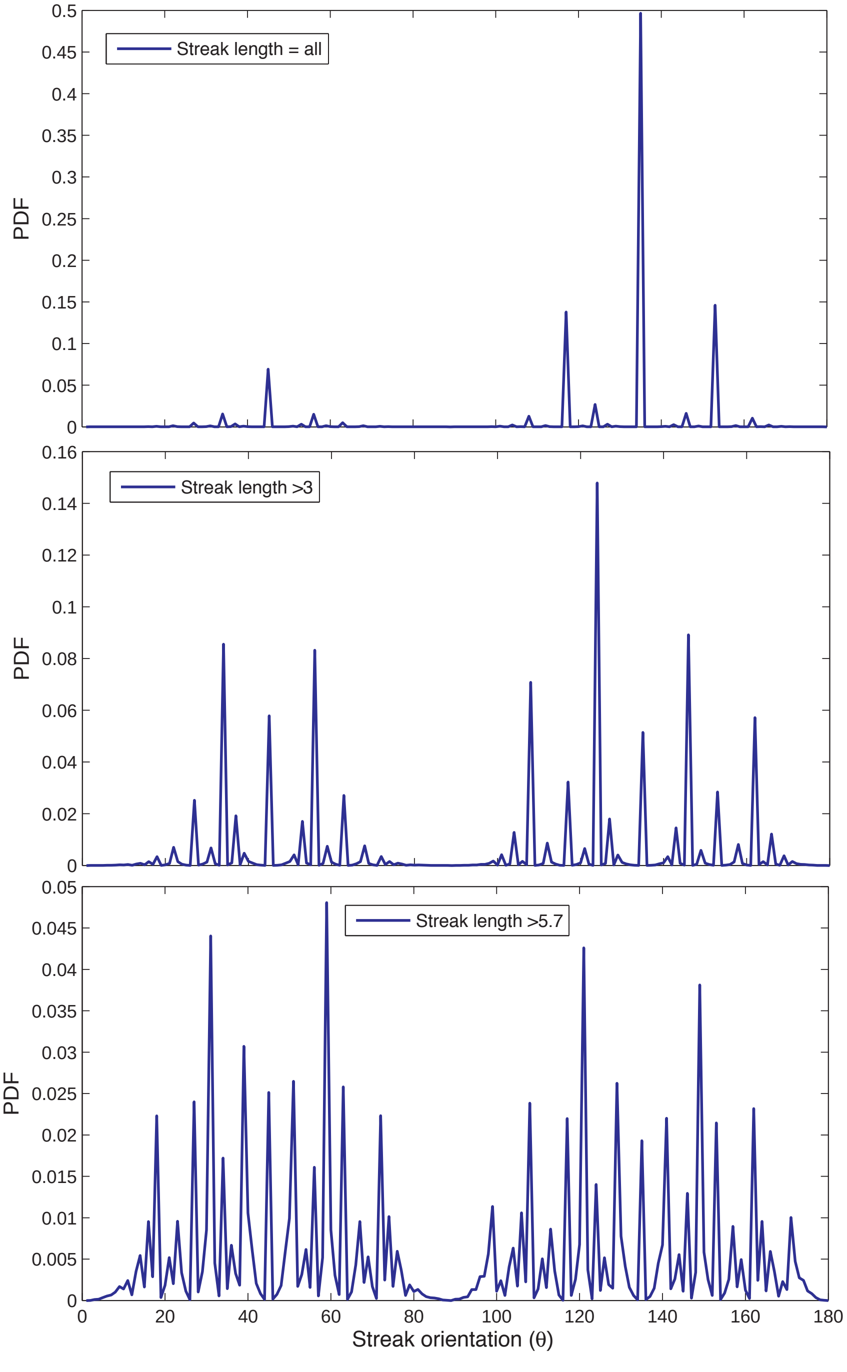

Fig. 26. PDF of Hubble orientations: (a) all pixel combination, (b) length cutoff filter equal to 3, (c) length cutoff filter equal to 5.7.

E. Proton streak simulations

This section describes Monte Carlo simulations that produced proton streak images with the underlying probability from Hubble. The results can be used to generate proton streak images that are not captured in space. This section also describes the Monte Carlo method used, the Metropolis algorithm implemented, and the statistical approach used to generate proton streak images.

The Monte Carlo method is a statistical approach that utilizes pseudorandom sampling to generate mathematical solutions. For problems with many coupled degrees of freedom, it is computationally heavy to discretize and solve for the exact solution. The Monte Carlo method can be used in those cases to map the solution by using generated pseudorandom variables [30]. The Metropolis algorithm, developed by Nicholas Metropolis in 1953, can be used to obtain variables from a known probability distribution [30, 31, 32]. This algorithm is used in this work to generate proton streaks lengths following the power law distribution determined from Hubble.

One of the key tools when using the Metropolis method is drawing pseudorandom variables from a uniform distribution. This distribution is one that is equally likely, i.e. such as the results of an unbiassed dice. One of the distributions in Figure (27), indicated by the diamond shape markers, is a uniform distribution for a variable λ between one hounded and one thousand, which plainly shows that the probability of a higher λ is equal to a smaller λ. The second distribution shown in Figure (27) is a power law, indicated by the circle markers, which is the desired distribution obtained from Hubble with a different exponent for purposes of visualization. The Metropolis algorithm uses a uniform distribution and the PDF of proton lengths from Hubble to draw a pseudorandom length from the power law distribution.

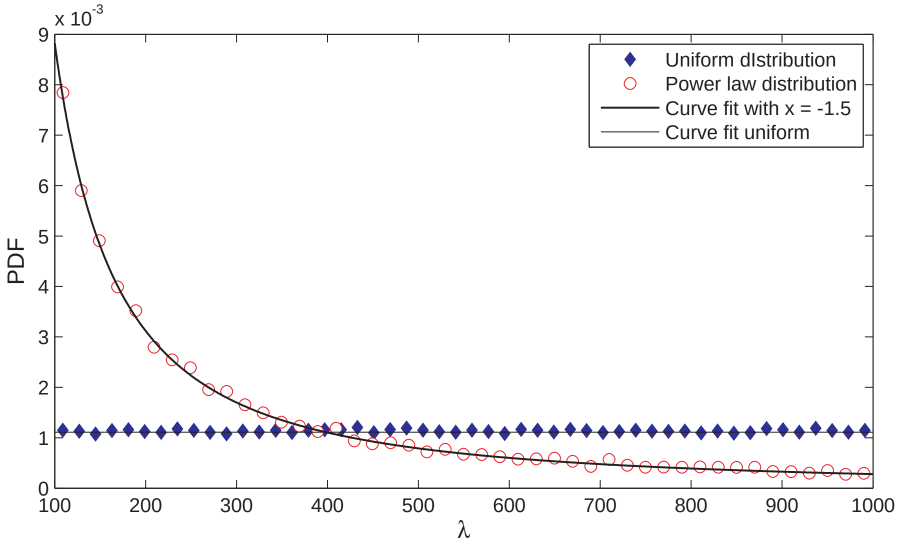

Fig. 27. Uniform distribution between 100 and 1000, and a power law distribution with exponent = -1.5, both are normalized to PDF.

The created simulation images are 8 bit images[12] with array size of 1024 × 1024 pixels, i.e. the same dimensions as the Hubble CCD. The starting location of the proton streak is found by choosing two pseudorandom numbers, y_i and x_i. These pseudorandom numbers are drawn from a uniform distribution. The image is in a rectangular coordinate system with a single integer number for each pixel. The image starts at $(0, 0)$ in the bottom left corner and is limited by the size of the image $(1023, 1023)$. Because of the limits of the image, the pseudorandom numbers y_i and x_i are bounded $(y_i = 0...1023, x_i = 0...1023)$.

The angle at which the proton streak is orientated on the image is found by choosing another pseudorandom number θ_i, from a uniform distribution, between zero and 2π. The orientation of the proton streak is measured from the horizontal x-axis.

---

[12] Minimum value of zero with a maximum value of $2^8 - 1 = 255$.

The Metropolis algorithm used to find the streak length starts by drawing a pseudorandom number for the length of the proton streak, L_1, between 2 and 1023. The streak length L_1 is put into the probability density function obtained from Hubble to get a relative likelihood of the length, $PDF_H(L_1) = C \times (L_1)^{-3.56}$. Subsequently, another pseudorandom number (L_2) is chosen between 0 and $PDF_H(2) \approx 0.67$ from a uniform distribution. The test to accept a streak length is $L_2 \leq PDF_H(L_1)$. If the test is true, the algorithm accepts the streak length L_1. If the test is false the streak length L_1 is rejected and the algorithm returns and chooses two new pseudorandom numbers for L_1 and L_2.

The block diagram for the Metropolis algorithm for proton streak generation is shown in Figure (28). This diagram illustrates that L_1 is first chosen from a pseudorandom number at block one, then passed to the relitive liklihood of that length in block two. Block three draws another pseudorandom number for L_2, which is passed to block four to check $L_2 \leq PDF_H(L_1)$ and accepts the streak length L_1 if true and rejects if false. The illustration also shows the pseudorandom numbers chosen for the starting location on the image y_i and x_i, and the orientation of proton streak θ_i.

Figures (29) and (30) show a Hubble image and a simulation image, which presents good visual correlation with the Hubble image. To quantify the correlation, one hundred simulation image were created, and streak length measurements were performed to acquire the PDF of proton lengths. The input power law coefficient -3.56 was put into the Metropolis algorithm with a resulting output coefficient equaling -3.85.

The difference between the Hubble data exponent and the simulations exponent could be due to the algorithm having to round values of lengths based on discreet pixels in the image. Since the difference in the coefficients is 0.29, the simulation

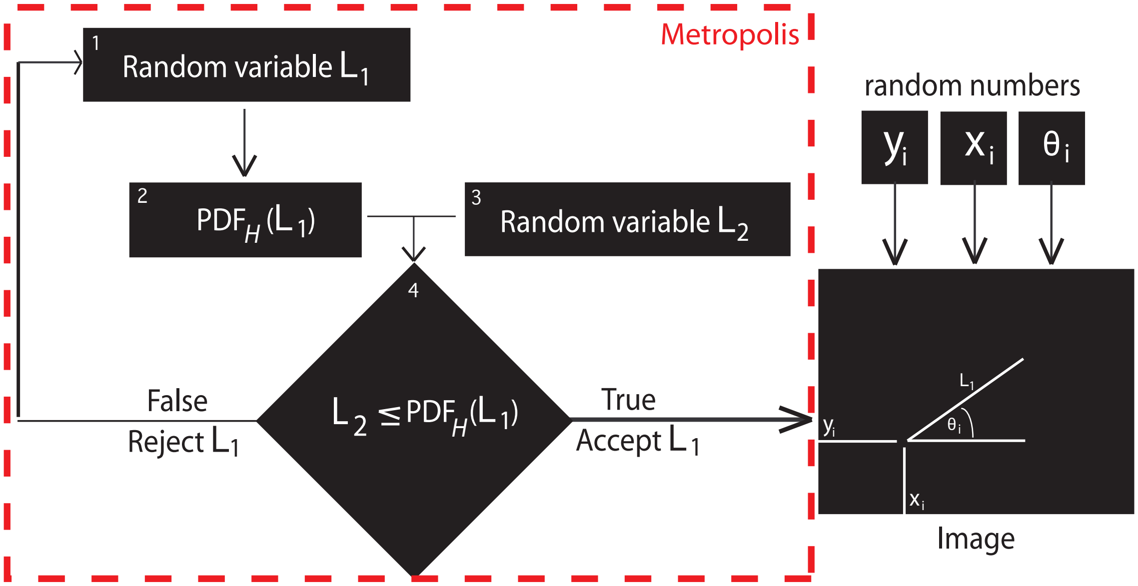

Fig. 28. Metropolis algorithm for streak length L_1.

can be considered an estimator for the actual sensor data. The result shows that the Metropolis algorithm is a good method for generating simulation images with proton streaks. This can be used in conjunction with other noise generating methods to create good synthetic images for space sensors to use for calibration and analysis.

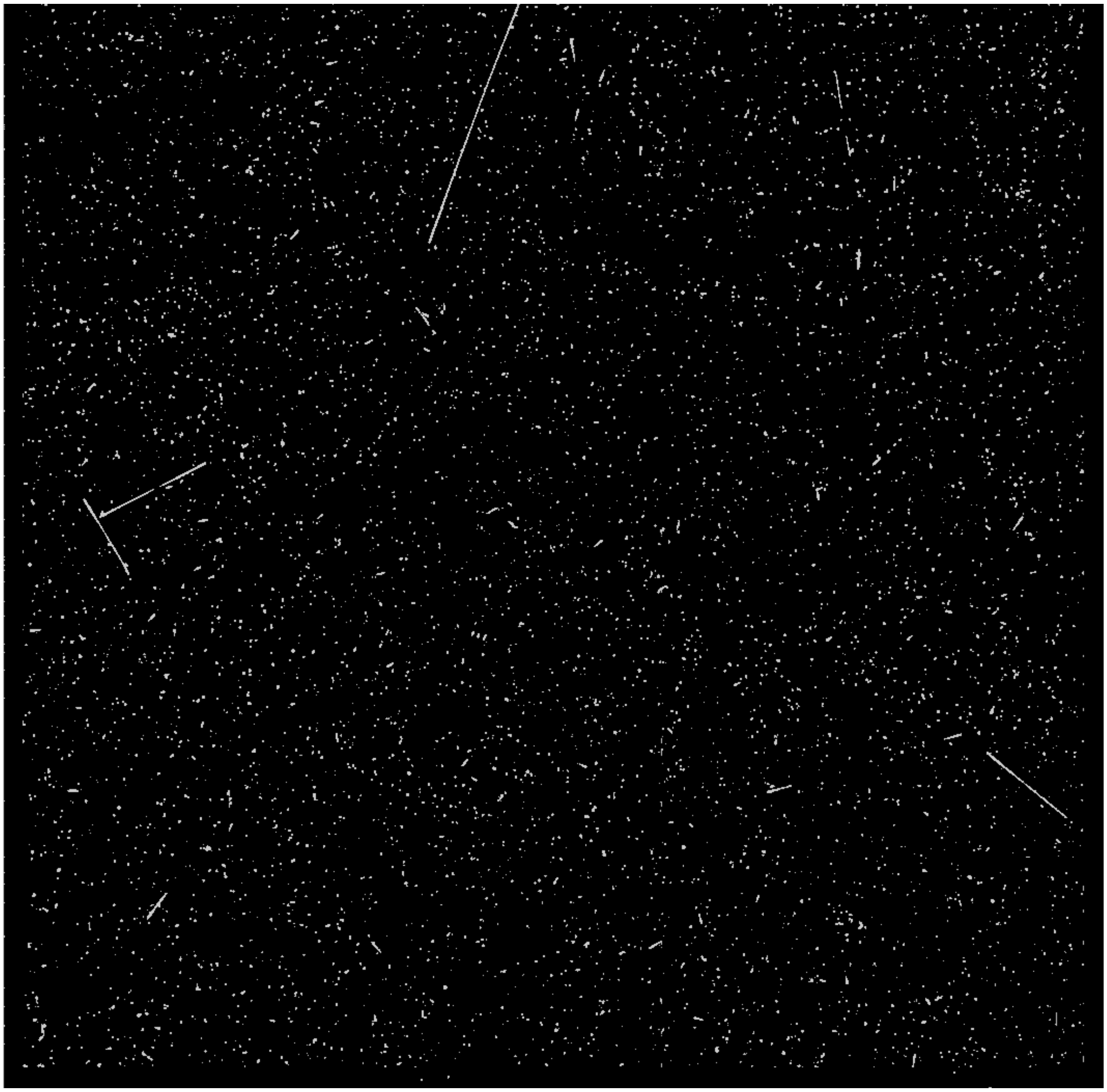

Fig. 29. Hubble image.

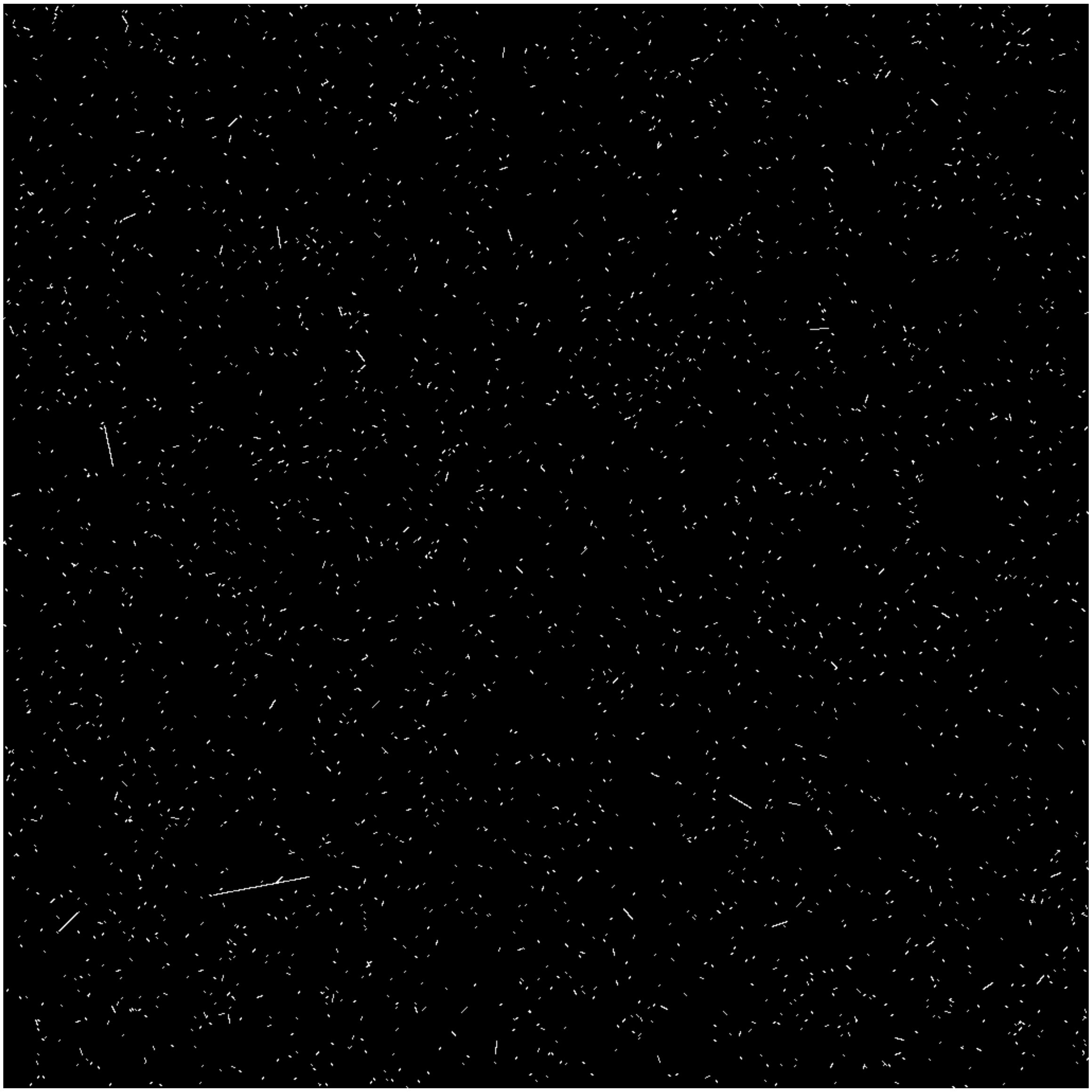

Fig. 30. Simulation image.

III. CONCLUSIONS

This thesis has presented an analysis of proton effects on an imaging CCD. Dark images with the presence of proton interactions from the Hubble Space Telescope were used. Statistical analysis of the images allowed us to examine the effect of space weather on a CCD. The Hubble was found to be a excellent source for dark images with proton events.

Protons arriving and transferring energy on the CCD are shown to follow a Poisson distribution, related to the rate at which the protons interact. This result quantifies the average amount of interacting proton events taking place on the CCD, while orbiting Low Earth Orbit (LEO) outside the South Atlantic Anomaly (SAA). By knowing the average flux of protons where the Hubble orbits, the predicted number of proton interactions with any satellite in LEO, with a similar inclination angle, can be calculated.

Protons deposit energy when they interact with the CCD structure. This interaction creates signal in the form of dark electrons. Different regions of the dark signal distribution are shown to follow a Gaussian distribution due to noise from the CCD, and an exponential distribution due to proton interactions.

Knowing that the exponential feature in the dark signal is due to proton interactions, proton streak lengths and angles can be measured in each image. The streak length distribution is shown to follow a power law, which is not dependent on the relative energy cutoff employed. The power law has been correlated to work by Henley [25] in order to create a model for streak lengths, which could be used to create noise images for any CCD with known parameters. Orientations of the proton events are also analyzed to find whether the space weather in LEO is directionally independent. The conclusion from this analysis is that the proton angles are isotropically distributed with higher probability of angles due to the power law and discrete pixels.

The statistics acquired from Hubble led to the generation of synthetic images, which follow the underlying probability statistics from Hubble. These simulated images can be used in conjunction with other noise simulations to create synthetic images that include all types of noise, including proton interactions, that can be used to calibrate space bound algorithms, e.g. star trackers, telescopes, ect. Images created on earth with noise that follows space weather in LEO could be used to lower the uncertainty for algorithms used in space-borne instruments.

REFERENCES

[1] K. Kudela, M. Storini, M. Y. Hofer, and A. Belov, “Cosmic rays in relation to space weather,” *Space Science Reviews*, vol. 93, pp. 152–174, 2000.

[2] D. N. Baker, M. Schussler, A. Warmuth, G. Mann, R. F. Wimmer-Schweingruber, A. Otto, G. W. Prolss, K. Schlegel, E. Valtonen, and J. Kiefer, *Space Weather: The Physics Behind a Slogan.* Heidelberg: Springer-Verlag, 2005.

[3] D. N. Baker, *Effects of Space Weather on Technology Infrastructure.* Dordrecht, The Netherlands: Kluwer Academic Publishers, 2004, vol. 176, ch. 1.

[4] J. W. Freeman, *Stroms in Space.* Cambridge, UK: Cambridge University Press, 2001.

[5] G. R. Hopkinson, “Cobalt60 and proton radiation effects on large format, 2-D, CCD arrays for an earth imaging application,” *IEEE Transactions on Nuclear Science*, vol. 39, no. 6, pp. 2018–2025, Dec. 1992.

[6] J. C. Pickel, R. A. Reed, R. Ladbury, B. Rauscher, P. W. Marshall, T. M. Jordan, B. Fodness, and G. Gee, “Radiation-induced charge collection in infrared detector arrays,” *IEEE Transactions on Nuclear Science*, vol. 49, no. 6, pp. 2822–2829, Dec. 2002.

[7] C. L. Howe, R. A. Weller, R. A. Reed, B. D. Sierawski, P. W. Marshall, C. J. Marshall, M. H. Mendenhall, R. D. Schrimpf, and J. E. Hubbs, “Distribution of proton-induced transients in silicon Focal Plane Arrays,” *IEEE Transactions on Nuclear Science*, vol. 54, no. 6, pp. 2444–2449, Dec. 2007.

[8] A. Theuwissen, *Solid-State Imaging with Charge-Coupled Devices.* Dordrecht, The Netherlands: Kluwer Academic Publishers, 1995.

[9] G. C. Messenger and M. S. Ash, *The Effects of Radiation on Electronic Systems.* New York: Van Nostrand Reinhold Company, 1986.

[10] J. R. Janesick, *Scientific Charge-Coupled Devices.* Bellingham, WA: SPIE-The International Society for Optical Engineering, 2001.

[11] C. J. Marshall and P. W. Marshall, "CCD radiation effects and test issues for satellite designers," NASA-GSFC Greenbelt, MD, Tech. Rep. 1, 2003.

[12] B. Nelson, M. Higashi, and P. Sharp, *Hubble Space Telescope: Servicing Mission 4 Media Reference Guide*, Lockheed Martin and NASA, Littleton, CO, 2008.

[13] M. Sirianni, M. Clampin, G. F. Hartig, H. C. Ford, G. D. Illingworth, V. Argabright, B. Burmester, G. D. Marchi, W. Koldewyn, A. R. Martel, M. Mutchler, A. Riess, R. J. Schrein, and P. C. Sullivan, "Characterization and on-orbit performance of the Advanced Camera for Surveys CCDs." *Proceedings of SPIE*, vol. 4854, pp. 496–506, 2003.

[14] M. Sirianni, M. Mutchler, M. Clampin, H. Ford, G. Illingworth, G. Hartig, D. Orsow, and T. Wheeler, "Performance of the Advanced Camera for Surveys CCDs after two years on orbit." *Proceedings of SPIE*, vol. 5499, pp. 173–184, 2004.

[15] M. Clampin, G. F. Hartig, H. C. Ford, M. Sirianni, G. Purdue, L. Walkowicz, D. A. Golimowski, G. Illingworth, M. Blouke, M. Lesser, B. Burmester, R. Kimble, P. C. Sullivan, and C. Krebs, "CCD detectors for the Advanced Camera for Surveys," *Proceedings of SPIE*, vol. 3356, pp. 332–337, 1998.

[16] T. N. Gautier and R. Gilliland, "Expected effects of hot CCD pixels on detection of transits of extra-solar planets with the Kepler mission," *Proceedings of SPIE*, vol. 5487, pp. 1572–1580, 2004.

[17] G. P. Ginet, D. Madden, B. K. Dichter, and D. H. Brautigam, "Energetic proton maps for the South Atlantic Anomaly," *IEEE Radiation Effects Data Workshop Record*, 2007.

[18] A. Papoulis and S. U. Pillai, *Probability, Random Variables and Stochastic Processes*, 4th ed. New York: McGraw-Hill, 2002.

[19] Hogg and Tains, *Probability and Statistical Inference*, 6th ed. Upper Saddle River, NJ: Prentice Hall, 1997.

[20] C. Pavlovsky, *ACS Data Handbook*, 3rd ed. Baltimore, MD: STScI, 2004.

[21] G. R. Hopkinson, "Proton effects in Charge-Coupled Devices," *IEEE Transactions on Nuclear Science*, vol. 43, no. 2, pp. 614–627, 1996.

[22] C. J. Marshall and P. W. Marshall, "Hot pixel annealing behavior in CCDs irradiated at $-84°$C," *IEEE Transactions on Nuclear Science*, vol. 52, no. 6, pp. 2672–2677, 2005.

[23] C. J. Marshall, P. W. Marshall, C. L. Howe, R. A. Reed, R. A. Weller, M. Mendenhall, A. Waczynski, R. Ladbury, and T. M. Jordan, "Comparison of measured dark current distributions with calculated damage energy distributions in HgCdTe," *IEEE Transactions on Nuclear Science*, vol. 54, no. 4, pp. 1097–1103, 2007.

[24] K. J. McCarthy, A. Owens, A. Wells, W. Hajdas, F. Mattenberger, and A. Zehnder, "Measured and modelled CCD response to protons in the energy range 50

to 300 MeV," *Nuclear Instruments and Methods*, vol. A361, no. 1, pp. 586–601, 1995.

[25] J. Henley, "Personal communication," April 2008.

[26] A. H. Kalma, "Analytical prediction of Gamma-induced pulse amplitude distributions in detectors," Mission Research Corporation, Colorado Springs, CO, Tech. Rep. DASG60-85-C-0063, Nov. 1988.

[27] S. Kirkpatrick, "Modeling diffusion and collection of charge from ionizing radiation in silicon devices," *IEEE Transactions on Electron Devices*, vol. ED-26, no. 11, pp. 1742–1753, Nov. 1979.

[28] G. P. Ginet, B. K. Dichter, D. H. Brautigam, and D. Madden, "Proton flux anisotropy in Low Earth Orbit," *IEEE Transactions on Nuclear Science*, vol. 54, no. 6, pp. 1975–1980, 2007.

[29] *NI Vision Concepts Manual*, National Instruments, Austin, Texas, 2008.

[30] J. M. Hammersley and D. C. Handscomb, *Monte Carlo Methods.* London: Spottiewoods, Ballantyne and Co Ltd, 1964.

[31] N. Metropolis, A. W. Rosenbluth, M. N. Rosenbluth, A. Teller, and E. Teller, "Equation of state calculations by fast computing machines," *Chemical Physics*, vol. 21, no. 6, pp. 1087–1092, 1953.

[32] W. Hastings, "Monte Carlo sampling methods using Markov chains and their applications," *Biometrika*, vol. 57, no. 1, pp. 97–109, 1970.

VITA

Name: Adam Alan Johnson

Address: Department of Aerospace Engineering
701 H.R. Bright Building, Ross St.- TAMU 3141
College Station, TX 77843-3141

Email Address: Adamfif@tamu.edu

Education: B.S., Aerospace Engineering, Texas A&M University, 2008
M.S., Aerospace Engineering, Texas A&M University, 2010

The typist for this thesis was Adam A. Johnson.